

Automation and control of laser wakefield accelerators using Bayesian optimisation

R.J. Shalloo*,¹ S.J.D. Dann,² J.-N. Gruse,¹ C.I.D. Underwood,³ A.F. Antoine,⁴ C. Arran,³ M. Backhouse,¹ C.D. Baird,^{3,2} M.D. Balcazar,⁴ N. Bourgeois,² J.A. Cardarelli,⁴ P. Hatfield,⁵ J. Kang,⁶ K. Krushelnick,⁴ S.P.D. Mangles,¹ C.D. Murphy,³ N. Lu,⁷ J. Osterhoff,⁸ K. Pöder,⁸ P.P. Rajeev,² C.P. Ridgers,³ S. Rozario,¹ M.P. Selwood,³ A.J. Shahani,⁷ D.R. Symes,² A.G.R. Thomas,⁴ C. Thornton,² Z. Najmudin,¹ and M.J.V. Streeter¹

¹*The John Adams Institute for Accelerator Science, Imperial College London, London, SW7 2AZ, UK*

²*Central Laser Facility, STFC Rutherford Appleton Laboratory, Didcot OX11 0QX, UK*

³*York Plasma Institute, Department of Physics, University of York, York YO10 5DD, UK*

⁴*Center for Ultrafast Optical Science, University of Michigan, Ann Arbor, MI 48109-2099, USA*

⁵*Clarendon Laboratory, University of Oxford, Parks Road, Oxford OX1 3PU, United Kingdom*

⁶*Department of Chemical Engineering, University of Michigan, Ann Arbor, MI 48109, USA*

⁷*Department of Materials Science and Engineering, University of Michigan, Ann Arbor, MI 48109, USA*

⁸*Deutsches Elektronen-Synchrotron DESY, Notkestr. 85, 22607 Hamburg, Germany*

(Dated: November 26, 2021)

Laser wakefield accelerators promise to revolutionise many areas of accelerator science [1]. However, one of the greatest challenges to their widespread adoption is the difficulty in control and optimisation of the accelerator outputs due to coupling between input parameters and the dynamic evolution of the accelerating structure. Here, we use machine learning techniques to automate a 100 MeV-scale accelerator, which optimised its outputs by simultaneously varying up to 6 parameters including the spectral and spatial phase of the laser and the plasma density and length. This led to significant improvements over manual optimisation, enhancing the electron and x-ray yields by factors of 3 or more, using only a few tens of measurements. Most notably, the model built by the algorithm enabled optimisation of the laser evolution that might otherwise have been missed in single-variable scans. Subtle tuning of the laser pulse shape caused a dramatic 80% increase in electron beam charge, despite the pulse length changing by just 1%.

In a laser wakefield accelerator (LWFA), an ultrashort intense laser pulse travelling through a plasma creates a wave in its wake which can be used to accelerate electrons to multi-GeV energies in just a few centimetres [2]. The enormous accelerating fields achievable in LWFAs could dramatically reduce the size and cost of future high-energy accelerators. In addition, the x-rays generated by transverse oscillations of electrons within the plasma structure can provide compact ultrafast synchrotron sources [3–5]. As such, there are a number of facilities based on LWFAs at various stages of planning, construction and operation [6–8]. In addition, there is now a global effort aimed at designing a compact plasma-based particle collider in lieu of, or even superseding, a future multi-10 km scale linear accelerator based on conventional technology [9].

In an LWFA, the laser pulse drives the plasma wave via the ponderomotive force, that depends on laser intensity, shape and spectral content. In general, all of these parameters are constantly evolving throughout the acceleration process. This is particularly evident in strongly-driven LWFAs where electrons are accelerated from within the plasma itself [10, 11]. Though it is possible to obtain simple expressions for the dependence of LWFA output on plasma density and laser intensity for an unchanging laser pulse [12], in reality, the evolution of laser parameters makes analytical treatment less tractable.

Furthermore, there are a large number of input parameters that must be tuned to optimise the accelerator performance, including those which affect the spatial and

spectral energy distribution of the laser pulse and those which control the nature of the plasma source. The usual approach to optimisation is to perform a series of single variable (1D) scans in the neighbourhood of the expected optimal settings. These scans are challenging, as the input parameters are often coupled and the highly sensitive response of the system can lead to large shot-to-shot variations in outputs. Moreover, due to the non-linear evolution of the LWFA, altering one input can affect the optimal values of all the other input parameters. Hence, sequential 1D optimisations do not reach the true optimum unless initiated there. A full N -D scan would be prohibitively time consuming for $N > 2$ and so a more intelligent search procedure is required.

Machine learning techniques are ideal for this kind of problem and have been demonstrated in other plasma physics, accelerator science and light source applications [13–16]. Genetic algorithms have been applied to laser-plasma sources including; using the spatial phase of the laser to optimise a keV electron source [17], and subsequently using both spectral and spatial phase to optimise a MeV-electron source [18]. In both cases, only the laser parameters were controlled preventing full optimisation of the LWFA which relies on the complex interplay between the laser and the plasma. Further, these optimisations did not incorporate the experimental errors and were therefore prone to distortion by statistical outliers.

In this paper, we present the use of Bayesian optimisation to demonstrate operation of the first fully automated laser-plasma accelerator. Simultaneous control of up to six laser and plasma parameters, enables indepen-

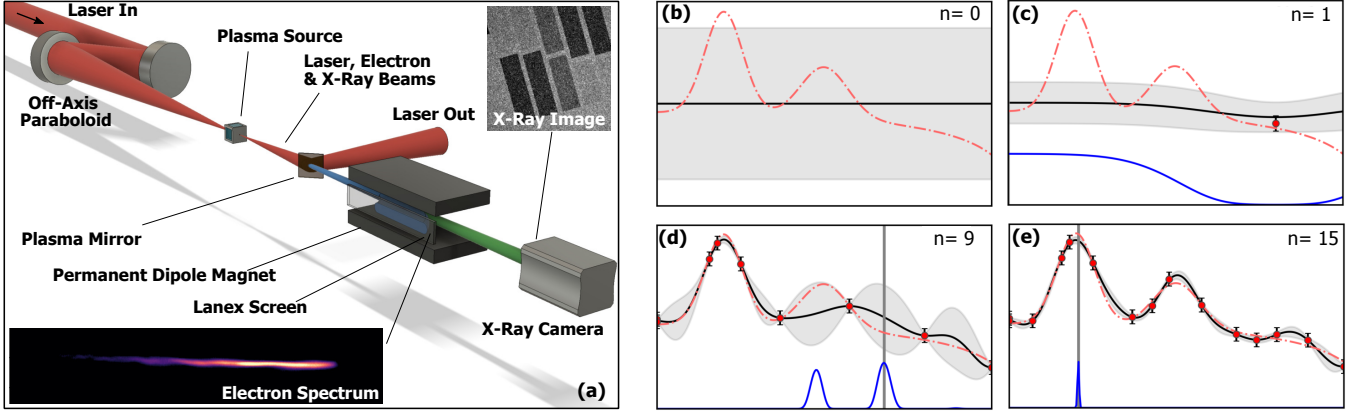


FIG. 1. **Experimental schematic and principle of Bayesian optimisation algorithm:** (a) Schematic of the laser-plasma accelerator showing an ultrashort, intense laser pulse focused into a plasma source. The laser drives a relativistic plasma wave, accelerating electrons to MeV energies and producing keV x-rays. The spectral and spatial phase of the laser pulse prior to focusing, and density and length of the plasma source could all be controlled programmatically. The electrons and x-rays were diagnosed by a permanent-dipole magnet spectrometer and a direct-detection x-ray camera respectively. (b-e) 1D example of Bayesian optimisation algorithm with $n = 0, 1, 9, 15$ measured data points. The dashed red line represents the true function, the black line represents the surrogate model and the gray shaded region denotes the error on the model. Data points are sampled from the true function with some error (red circles). As more data points are added, the surrogate model begins to more closely resemble the true function. The blue line represents the acquisition function, the maximum of which, tells the algorithm which point to sample next.

dent optimisation of different properties of the source far exceeding that achieved manually. In performing the optimisation, the algorithm builds a surrogate model of the parameter space, including the uncertainty arising from the sparsity of the data and the measurement variances. By interrogation of this model, we discover physically important correlations between experimental parameters demonstrating that new physics may be discovered via machine-learning-based optimisation.

I. BAYESIAN OPTIMISATION

Bayesian optimisation is a popular and efficient machine learning technique for the multivariate optimisation of expensive to evaluate or noisy functions [19, 20]. At its core, it creates a surrogate model of the *objective function* (the observable to be optimised), which is then used to guide the optimisation process. The model is a prior probability distribution over all possible objective functions, representing our belief about the function’s properties such as amplitude and smoothness. This distribution is commonly realised as a Gaussian process model in a technique called Gaussian Process Regression (GPR) [21]. The prior distribution is updated with each new measurement to produce a more accurate posterior distribution. The mean of this distribution (the black line in fig. 1(b-e)) is our best estimate of the objective function’s form (the red dashed line in fig. 1(b-e)), and its maximum gives the best estimate of the maximum of the real objective function.

Every function sampled from the posterior distribution

will be compatible with the measurements used to construct it. In the case where the measurements have some variance associated with them, this information can also be fed into the posterior distribution; such that functions sampled from the posterior distribution need only fit the data to the precision dictated by their uncertainty. Using this approach, the model includes both uncertainty and correlations between measurements at different points. The correlation between any two points in the space is characterised by the *covariance kernel*.

Our Bayesian optimisation procedure is conceptually depicted in fig. 1 (b-e) and proceeded as follows:

1. A Gaussian process model is constructed, using a physically sensible form for the covariance kernel.
2. A number of experimental measurements are made at chosen positions to initialise the algorithm.
3. The model is updated with the accumulated measurements to form a posterior distribution.
4. An *acquisition function* is computed (see below), and used to select the next measurement location.
5. Steps 3-4 are repeated until the convergence criteria are met.

The next point to be sampled is determined by an acquisition function based on the mean, μ , and standard deviation, σ , of the model. This allows for a trade-off between exploring parts of the domain where few measurements have been made (σ is high) and exploiting parts of the domain believed to be near a maximum (μ is high). A simple example acquisition function is the upper confidence bound, $UCB = \mu + \kappa\sigma$, where κ characterises the trade-off between exploration and exploitation.

In the work performed here, an augmented Bayesian

optimisation procedure, developed by the authors but based on the *scikit-learn* platform [22], was utilised. This algorithm included two GPR models, to allow for efficient sampling of the parameter space in the presence of input-dependent measurement uncertainty (see methods for details).

II. EXPERIMENTAL SETUP

The experiments were performed with the Gemini TA2 Ti:sapphire laser system at the Central Laser Facility, using the arrangement shown in fig. 1a. On target, each laser pulse contained approximately 245 mJ, had a 45 fs transform limit and was focused to a $1/e^2$ spot radius of 16 μm for a peak normalised vector potential of $a_0 = 0.55$. Despite, its relatively modest specifications, the laser can be used to drive a 100 MeV-class LWFA at 1 Hz, with a gas cell acting as the plasma source.

The relevant outputs of the source were measured at the exit of the plasma by standard diagnostics; an electron spectrometer to measure energy distribution, charge and beam profile of the accelerated electrons, and an x-ray camera that measures yield, energy and divergence of generated betatron x-rays.

The optimisation algorithm was used to control this accelerator by manipulating the spectral and spatial phase profiles of the laser pulse as well as the length and electron density of the plasma. The spectral phase of the laser pulse $\phi(\omega)$ was controlled by an acousto-optic programmable dispersive filter (AOPDF) allowing for variation of the temporal profile of the compressed laser pulse. The changes to the spectral phase were parameterised by the coefficients of a polynomial $\phi(\omega) = \sum (\omega - \omega_0)^n \beta^{(n)} / n!$, with $\beta^{(n)} = 0$ corresponding to optimal compression. The 2nd, 3rd and 4th orders ($\beta^{(2)}, \beta^{(3)}, \beta^{(4)}$) were independently controlled by the algorithm. A piezoelectric deformable mirror provided control over the spatial phase of the laser pulse, allowing the algorithm to apply deformations to the wavefront, for example to shift the focal plane relative to the electron density profile. The electron density of the plasma was controlled by changing the pressure of a gas reservoir connected directly to the plasma source. Modification of the length of the plasma source was achieved by changing the length of the custom-designed gas cell.

Every element of the optimisation, the control, analysis and selection of the next evaluation point, proceeded automatically without input from the user. For each measurement, a single burst comprising 10 shots was taken. Each diagnostic was analysed and the results were used to calculate the objective function. Taking 10 shots allowed for calculation of the mean and variance of the objective function for a given set of input parameters. During the optimisation runs, all selected parameters were free to vary simultaneously and so were all optimised concurrently.

III. OPTIMISATION OF ELECTRON AND X-RAY PRODUCTION

We demonstrate the optimisation algorithm by using a simple objective function; the total counts recorded by the electron spectrometer. This corresponds to the total charge in the laser-generated electron beam with $E = \gamma m_e c^2 > 26 \text{ MeV}$. To demonstrate the robustness of the optimisation, 10 consecutive optimisation runs were performed using the same algorithm. A gas mixture of 1% nitrogen and 99% helium was used to allow for ionisation injection [23–25] providing a reduced threshold for electron beam generation compared to pure helium. The optimisation varied four input parameters; the spectral phase coefficients $\beta^{(2)}$, $\beta^{(3)}$ and $\beta^{(4)}$ and the longitudinal position of focus of the laser pulse f . The first measurement point for each run was taken at the optimum position from the previous days operation. Due to the drift of laser performance and experimental parameters, optimal positions varied day to day.

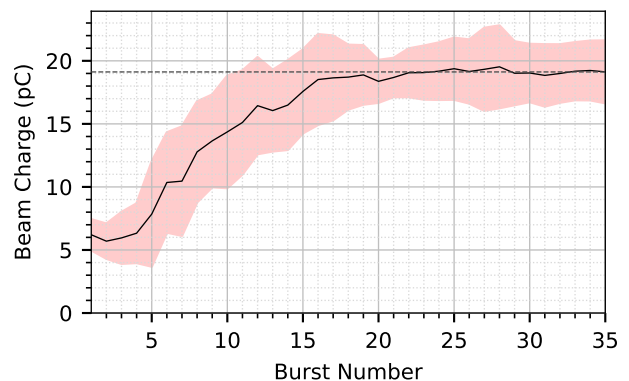


FIG. 2. **Convergence test of 10 identical optimisation runs:** The maximum predicted electron beam charge (for $\gamma m_e c^2 > 26 \text{ MeV}$) across the 10 runs is plotted as a function of burst number (10 shots per burst). The shaded region encloses \pm a standard deviation of uncertainty. The runs were performed in a nitrogen-helium gas mix.

In order to track the progress of the algorithm during each optimisation, we obtained the surrogate model's prediction of the global maximum after each burst. The average and standard deviation of this predicted optimum over the 10 runs is plotted in fig. 2. The algorithm was able to optimise electron beam charge in 4D with just 20 measurements, consisting of 200 total shots and taking 6.5 minutes including the time for parameter setting and computation. In each case, the final optimum value (indicated by the dashed line) was reached after approximately 20 bursts, resulting in a 3 times increase in electron beam charge. After this point, the local maximum has been fully exploited and the algorithm continued to explore other parts of the parameter space where statistical uncertainty of the model was largest. The change in parameters from the starting point to the optimum was -60 fs^2 , $9 \times 10^3 \text{ fs}^3$, $6 \times 10^5 \text{ fs}^4$ and 0.7 mm for $\beta^{(2)}$, $\beta^{(3)}$,

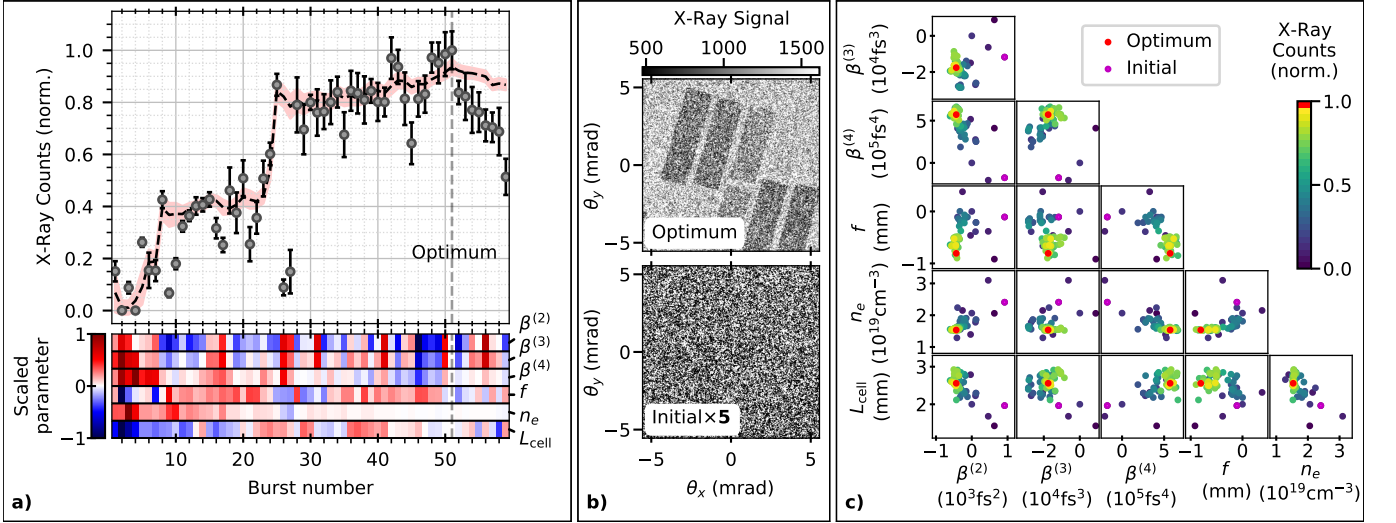


FIG. 3. **6-D Optimisation of betatron x-ray source:** a) Top panel shows the mean (normalised) x-ray yield for each burst (circles) with standard error. The dashed line shows the model predicted maximum value of x-ray yield with the shaded region enclosing \pm standard deviation uncertainty. The lower panel shows the evolution of the input parameters representing the focal position of the laser pulse (f), the plasma electron density (n_e), the plasma source length (L_{cell}) and three orders of spectral phase ($\beta^{(2)}$, $\beta^{(3)}$, $\beta^{(4)}$). b) X-ray images from the initial and optimal bursts, where the signal for each pixel is the mean from the 10 individual shots. The initial x-ray image is multiplied by 5 to make it visible on the same scale. c) The projection of the measurements onto each 2D plane of the parameter space, colour coded by the normalised total x-ray counts.

$\beta^{(4)}$ and f respectively.

For a more challenging optimisation, we chose the yield of betatron x-rays as the objective function. Maximising the flux of these ultra-short bursts of x-ray radiation would be of great benefit for a diverse range of applications, such as the imaging of medical, industrial and scientific samples [5]. The x-rays from an LWFA can be emitted at any point in the accelerator where the electrons reach a high energy and oscillate with a large amplitude. These electrons may subsequently decelerate such that they are not detected by the electron spectrometer, and so the x-ray flux may be optimised by substantially different input parameters than those which optimised the measured electron beam charge.

An example is shown in fig. 3a, where the total x-ray yield, characterised as counts on the x-ray camera, was optimised in a pure helium plasma. Six input parameters were varied, incorporating the backing pressure and length of the gas cell. Here a five fold increase in x-ray yield is achieved in a 27 minute 6D optimisation. This results in a dramatic increase in the usability of the x-ray source, as shown in fig. 3b where the filter array becomes clearly visible. This is notable since the energy of this laser system would usually be considered inadequate for betatron imaging applications.

The bottom panel of fig. 3a shows how the input parameters were varied for each burst to achieve the indicated x-ray yield. For the purposes of this visualisation, the input parameters are offset so that the optimum position is at 0, and scaled so that all values lie in the range ± 1 . The pair-plots of the measurement positions, shown in fig. 3c, show how each parameter varied and

were guided towards the local optimum. The initial position was the optimum from the previous days operation, for which the laser performance was significantly different, including lower pulse energy. The optimisation was able to tune the laser compression and focusing, and also found increased performance by operating at a lower plasma density and longer gas cell length.

IV. TAILORING ELECTRON BEAM CHARACTERISTICS

A strength of a fully automated LWFA is that the highly flexible accelerator can be tailored to specific applications merely by changing the objective function. For example, for the generation of positron beams [26] or gamma-rays [27, 28], it is advantageous to prioritise the conversion of laser energy to electron beam energy. By contrast, for sending the output of the LWFA to a second acceleration stage [29], fine control of the electron beam divergence and energy spread is more important. Careful selection of this objective function is vital and can be used to control the phase space of the beams.

In defining the objective function, any combination of measurable quantities may be used as long as they can be expressed as a single number with a good estimate of the measurement error. Here the results of two additional optimisations based on more complex objective functions are presented; one targeting total electron beam energy (*example A*) and the other, the electron beam divergence (*example B*). In both cases the gas cell was filled with helium doped with 1% nitrogen to allow for ionisation

injection. The gas cell length was fixed in each example prior to optimisation reducing the automated optimisations to 5D.

For *example A*, the initial conditions were seen to be far from optimal and during the 20 minute, 5D optimisation, all five input parameters had to vary significantly to achieve the optimum, a 24 times increase in the average value of total beam energy to 0.96 ± 0.16 mJ. For *example B*, an objective function was employed which only summed charge within a 3.75 mrad acceptance angle around the laser axis. This *rewarded* electron beams with a high charge per unit divergence which were well aligned to this central axis. This optimisation gave a minimum burst-averaged electron beam divergence of 3.4 ± 0.2 mrad, while the total beam energy was lower than in *example A* at 0.27 ± 0.04 mJ.

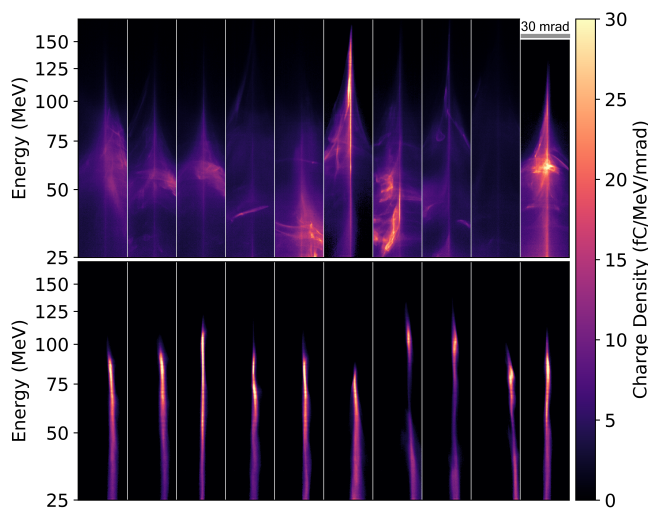


FIG. 4. **Angularly resolved electron spectra for different objective functions:** A burst (ten consecutive shots) optimised for: (*example A* - top) total electron beam energy; (*example B* - bottom) electron beam divergence obtained by counting charge within a 3.75 mrad acceptance angle.

Both optimisations achieved the maximum values of their objective functions within 40 bursts. Figure 4 shows ten consecutive beams from the best burst of each of the two optimisations. There is a clear distinction in the form of the optimal electron beams for the two cases. This demonstrates the fundamental impact that the choice of objective function has on the accelerator performance. It also shows the importance of choosing the correct objective function for a given application, as although the total beam charge for *example B* is lower, it is far more suitable for some applications, for example if the beam is required to pass through a narrow collimator to an interaction chamber.

While the qualitative features of the beams in fig. 4 are consistent in each of the two bursts, it is clear that there is also shot-to-shot variation in the spectra of the beams for nominally identical conditions. This variation can be primarily attributed to the stability of the laser sys-

tem, which had peak-to-valley fluctuations in the pulse energy of 8%, the pulse duration of 6% and focal position of a Rayleigh length (1 mm). It is a testament to the Bayesian-optimisation-based approach that optima could be reliably located despite the shot-to-shot fluctuations in parameters. Implementing these automated optimisation techniques on next generation laser systems, which demonstrate significantly higher stability in the laser parameters [30], will result in much finer tuning and control of the electron and x-ray beams.

V. EXPLORING THE MODELS

The model constructed by the optimisation algorithm describes the behaviour of the physical system with increasing accuracy as more measurements are taken. In the case of the optimisation convergence runs discussed in section III, 350 measurements, consisting of 3500 shots, were combined from ten runs to generate a model of the 4D parameter space. By investigating this model, a clear correlation was observed between two of the input parameters, the second $\beta^{(2)}$ and fourth $\beta^{(4)}$ order components of the spectral phase. This can be clearly seen by taking a 2D slice through the 4D parameter space as shown in fig. 5a.

The correlation between $\beta^{(2)}$ and $\beta^{(4)}$ is a consequence of expressing the spectral phase as a polynomial, i.e. even orders are mathematically coupled. The chirp of the laser pulse due to the introduction of $+\beta^{(2)}$ can be partially compensated by $-\beta^{(4)}$, maintaining a high peak power. For a laser with spectral bandwidth $\Delta\omega$, the change in group delay at $\omega_0 \pm \Delta\omega$ cancels out when $\Delta\beta^{(4)} = -6\Delta\beta^{(2)}/(\Delta\omega)^2$. The solid and dashed lines in fig. 5a represent this relationship using the measured FWHM bandwidth and matches the observed gradient of the correlation. The dashed line shows the case of a fully compressed pulse, while the solid line represents a pulse with a fixed amount of positive chirp. Along the solid line, which passes through the optimum of the trained surrogate model, the charge produced by the LWFA remains high for a significant change in spectral phase coefficients. Previous observations have also determined that a positive chirp is advantageous for self-injection in a 1D scan of $\beta^{(2)}$ [31]. Here, we find that a small amount of positive chirp is optimal for ionisation injection also, and that subtle changes to the laser pulse shape, using a combination of $\beta^{(2)}$ and $\beta^{(4)}$, maximise this enhancement. The large change in charge is remarkable, considering that the standard measure of laser pulse length, the FWHM, changed by only 0.5 fs in this optimisation.

Simulations were performed using the quasi-3D particle-in-cell (PIC) code FBPIC [32] to understand the reason for the observed behaviour. The laser pulse was initialised to match experimental measurements of the transverse intensity profile and the temporal intensity and phase. The peak vacuum a_0 was set to 0.55 ensuring that the integral of the laser energy distribution was

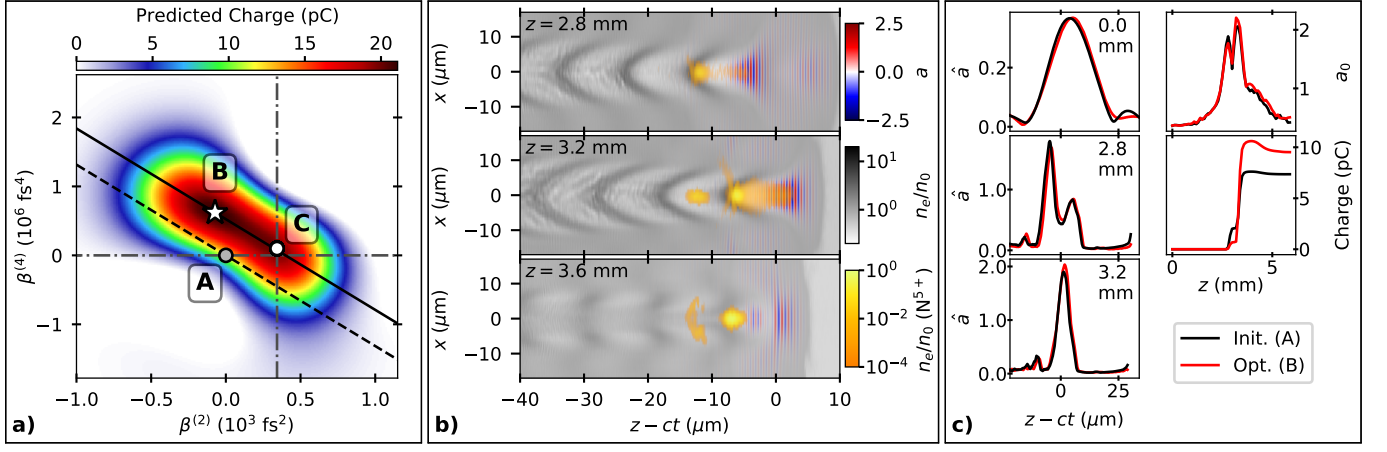


FIG. 5. **Electron beam charge optimisation through pulse shaping:** a) Surrogate model predicted charge as a function of $\beta^{(2)}$ and $\beta^{(4)}$, for the optimal values of $\beta^{(3)}$ and f . Markers show the initial (A) and optimal (B) positions and the likely end result of sequential 1-D optimisations of $\beta^{(2)}$ and $\beta^{(4)}$ (C). The diagonal lines show the combination of $\beta^{(2)}$ and $\beta^{(4)}$ modifications that maintain an approximately constant pulse shape. b) Snapshots from a PIC simulation showing the laser normalised vector potential a , the electron densities of the background plasma and the electrons released from the two inner ionisation levels of nitrogen normalised to $n_0 = 1.2 \times 10^{19} \text{ cm}^{-3}$. c) (Left) Axial laser field envelope at the given z positions and (right) maximum laser field and total electron beam charge as functions of z position from simulations using the input laser pulse spectral phase coefficients from points A and B from a).

equal to the average pulse energy of this run (0.245 J).

After entering the plasma, the driving laser pulse undergoes self-focusing, self-modulation and self-compression (as shown in fig. 5b) increasing the intensity of the pulse. This causes further ionisation of the nitrogen dopant in the plasma, the inner two shells of which require $a \geq 1.9$ to field-ionise. This occurs primarily at $z = 3.2 \text{ mm}$, where a large fraction of the inner shell electrons are trapped within the accelerating structure.

Figure 5c shows how very small differences in the initial pulse temporal profiles at $z = 0.0$ can grow as a result of the non-linear behaviour. Before entering the plasma, the optimal positively chirped pulse (B) had a slightly sharper rising edge than the unchirped pulse (A), but the same peak intensity. During the initial self-focusing stage ($z = 2.8 \text{ mm}$), the peak a_0 of pulse A evolved to be 7% higher than pulse B. Subsequently, self-modulation and pulse compression created a second higher intensity spike forming at $z = 3.6 \text{ mm}$, where the a_0 of pulse B peaked 7% higher than pulse A. This is the point at which the majority of injection occurred, and so more charge was trapped for the case of the optimal positively chirped pulse (B).

Figure 5a also shows the consequences if the experiment was instead optimised by two sequential 1D scans of $\beta^{(2)}$ and then $\beta^{(4)}$. In this case, the correlation of these two parameters is not found and the final optimum (C) is significantly removed from the true optimum, although only slightly lower in predicted charge; the increase in charge for 1D scans is 87% of the increase between the initial and true optimal positions. The potential loss in performance is compounded with every additional di-

mension considered, especially where the initial position might be further from the optimum. Comparison of different optimisation algorithms within this 4D parameter space (see methods) using Monte-Carlo simulations show that Bayesian optimisation significantly outperforms sequential 1D optimisations, as well as optimisations using genetic or Nelder-Mead algorithms. To perform a 4D grid search of this parameter space would take an impractical 14641 measurements (11 measurements per dimension) to obtain the same performance as the Bayesian optimisation algorithm.

VI. CONCLUSION

In this paper, we have presented a new fully automated Bayesian approach to the optimisation and control of LWFA. Through the generation of a surrogate model, the algorithm was able to modify the experimental controls and quickly optimise the generated electron and x-ray beams. Interrogation of one of the generated models also provided physical insight into the dynamics of the electron injection process. It is envisaged, that by using this optimisation-led approach to learn about complex interactions, unexpected behaviours can be discovered and used to inform the design of better future plasma accelerators. The correct choice of objective function for the optimisation algorithm also allows for the nature of the plasma source to be fundamentally altered, enabling a single device to serve many different potential applications. This could be further exploited by using the application itself to provide the objective function, for example coherent x-ray production from a LWFA driven

free-electron laser. It is anticipated that the first generation of laser-plasma accelerator user facilities will need

to make use of automated global optimisation in order to maximise their competitiveness.

-
- [1] S. M. Hooker, *Nature Photonics* **7**, 775 (2013).
- [2] A. J. Gonsalves, K. Nakamura, J. Daniels, C. Benedetti, C. Pieronek, T. C. H. de Raadt, S. Steinke, J. H. Bin, S. S. Bulanov, J. van Tilborg, C. G. R. Geddes, C. B. Schroeder, C. Tóth, E. Esarey, K. Swanson, L. Fan-Chiang, G. Bagdasarov, N. Bobrova, V. Gasilov, G. Korn, P. Sasorov, and W. P. Leemans, *Physical Review Letters* **122**, 084801 (2019).
- [3] S. Fourmaux, S. Corde, K. T. Phuoc, P. Lassonde, G. Lebrun, S. Payeur, F. Martin, S. Sebban, V. Malka, A. Rousse, and J. C. Kieffer, *Optics Letters* **36**, 2426 (2011).
- [4] S. Kneip, C. McGuffey, J. L. Martins, S. F. Martins, C. Bellei, V. Chvykov, F. Dollar, R. Fonseca, C. Huntington, G. Kalintchenko, A. Maksimchuk, S. P. Mangles, T. Matsuoka, S. R. Nagel, C. A. Palmer, J. Schreiber, K. T. Phuoc, A. G. Thomas, V. Yanovsky, L. O. Silva, K. Krushelnick, and Z. Najmudin, *Nature Physics* **6**, 980 (2010).
- [5] F. Albert and A. G. Thomas, *Plasma Physics and Controlled Fusion* **58**, 103001 (2016).
- [6] *EuPRAXIA Conceptual Design Report*, Tech. Rep. (The EuPraxia Consortium, 2020).
- [7] S. Jacquemot and P. Zeitoun, in *X-Ray Lasers and Coherent X-Ray Sources: Development and Applications XIII*, Vol. 11111, edited by A. Klisnick and C. S. Menoni, International Society for Optics and Photonics (SPIE, 2019).
- [8] B. Rus, F. Batysta, J. Āņāp, M. Divokāj, M. Fibrich, M. Griffiths, R. Haley, T. HavlāņĀĎek, M. Hlavāq, J. HāŽebāņĀĎek, P. Homer, P. HāŽāņbek, J. Jand'ourek, L. Juha, G. Korn, P. Korouāq, M. Koāqelja, M. Kozlovāq, D. Kramer, M. Krārs, J. C. Lagron, J. Limpouch, L. MacFarlane, M. Malāj, D. Margarone, P. Matlas, L. Mindl, J. Moravec, T. Moecek, J. Nejd, J. Novāq, V. Olāqovcovāq, M. Palatka, J. P. Perin, M. Peāqlo, J. Polan, J. Prokārppek, J. ĀYāņdkāj, K. Rohlena, V. RāfājiāĎka, M. Sawicka, L. Scholzovāq, D. Snopek, P. Strkula, and L. Āāvāfda, in *Diode-Pumped High Energy and High Power Lasers; ELI: Ultrarelativistic Laser-Matter Interactions and Petawatt Photonics; and HiPER: the European Pathway to Laser Energy*, Vol. 8080, edited by L. O. Silva, G. Korn, L. A. Gizzi, C. Edwards, and J. Hein, International Society for Optics and Photonics (SPIE, 2011) pp. 163 – 172.
- [9] B. Cros and P. Muggli, “Alegro input for the 2020 update of the european strategy,” (2019), [arXiv:1901.08436 \[physics.acc-ph\]](https://arxiv.org/abs/1901.08436).
- [10] M. J. V. Streeter, S. Kneip, M. S. Bloom, R. A. Bendoyro, O. Chekhlov, A. E. Dangor, A. Döpp, C. J. Hooker, J. Holloway, J. Jiang, N. C. Lopes, H. Nakamura, P. A. Norreys, C. A. J. Palmer, P. P. Rajeev, J. Schreiber, D. R. Symes, M. Wing, S. P. D. Mangles, and Z. Najmudin, *Phys. Rev. Lett.* **120**, 254801 (2018).
- [11] E. Esarey, B. A. Shadwick, C. B. Schroeder, and W. P. Leemans, *AIP Conference Proceedings* **737**, 578 (2004), <https://aip.scitation.org/doi/pdf/10.1063/1.1842594>.
- [12] W. Lu, C. Huang, M. Zhou, M. Tzoufras, F. S. Tsung, W. B. Mori, and T. Katsouleas, *Physics of Plasmas* **13**, 056709 (2006).
- [13] A. Radovic, M. Williams, D. Rousseau, M. Kagan, D. Bonacorsi, A. Himmel, A. Aurisano, K. Terao, and T. Wongjirad, *Nature* **560**, 41 (2018).
- [14] C. Emma, A. Edelen, M. J. Hogan, B. O'Shea, G. White, and V. Yakimenko, *Physical Review Accelerators and Beams* **21**, 112802 (2018).
- [15] J. A. Gaffney, S. T. Brandon, K. D. Humbird, M. K. Kruse, R. C. Nora, J. L. Peterson, and B. K. Spears, *Physics of Plasmas* **26**, 082704 (2019).
- [16] J. Duris, D. Kennedy, A. Hanuka, J. Shtalenkova, A. Edelen, P. Baxevanis, A. Egger, T. Cope, M. McIntire, S. Ermon, and D. Ratner, *Physical Review Letters* **124**, 124801 (2020).
- [17] Z.-H. He, B. Hou, V. Lebailly, J. A. Nees, K. Krushelnick, and A. G. R. Thomas, *Nature Communications* **6**, 7156 (2015).
- [18] S. J. D. Dann, C. D. Baird, N. Bourgeois, O. Chekhlov, S. Eardley, C. D. Gregory, J.-N. Gruse, J. Hah, D. Hazra, S. J. Hawkes, C. J. Hooker, K. Krushelnick, S. P. D. Mangles, V. A. Marshall, C. D. Murphy, Z. Najmudin, J. A. Nees, J. Osterhoff, B. Parry, P. Pourmoussavi, S. V. Rahul, P. P. Rajeev, S. Rozario, J. D. E. Scott, R. A. Smith, E. Springate, Y. Tang, S. Tata, A. G. R. Thomas, C. Thornton, D. R. Symes, and M. J. V. Streeter, *Phys. Rev. Accel. Beams* **22**, 041303 (2019).
- [19] J. Mockus, *Control and Information Sciences* **38**, 473 (1982).
- [20] B. Shahriari, K. Swersky, Z. Wang, R. P. Adams, and N. de Freitas, *Proceedings of the IEEE* **104**, 148 (2016).
- [21] C. E. Rasmussen and C. K. I. Williams, *Gaussian Processes for Machine Learning (Adaptive Computation and Machine Learning)* (The MIT Press, 2005).
- [22] F. Pedregosa, G. Varoquaux, A. Gramfort, V. Michel, B. Thirion, O. Grisel, M. Blondel, P. Prettenhofer, R. Weiss, V. Dubourg, J. Vanderplas, A. Passos, D. Cournapeau, M. Brucher, M. Perrot, and E. Duchesnay, *Journal of Machine Learning Research* **12**, 2825 (2011).
- [23] T. P. Rowlands-Rees, C. Kamperidis, S. Kneip, A. J. Gonsalves, S. P. D. Mangles, J. G. Gallacher, E. Brunetti, T. Ibbotson, C. D. Murphy, P. S. Foster, M. Streeter, F. Budde, P. A. Norreys, D. A. Jaroszynski, K. Krushelnick, Z. Najmudin, and S. M. Hooker, *Physical Review Letters* **100**, 105005 (2008).
- [24] A. Pak, K. A. Marsh, S. F. Martins, W. Lu, W. B. Mori, and C. Joshi, *Physical Review Letters* **104**, 025003 (2010).
- [25] C. McGuffey, A. G. R. Thomas, W. Schumaker, T. Matsuoka, V. Chvykov, F. J. Dollar, G. Kalintchenko, V. Yanovsky, A. Maksimchuk, K. Krushelnick, V. Y. Bychenkov, I. V. Glazyrin, and A. V. Karpeev, *Phys. Rev. Lett.* **104**, 025004 (2010).
- [26] G. Sarri, K. Poder, J. M. Cole, W. Schumaker, A. Di Piazza, B. Reville, T. Dzelzainis, D. Doria, L. A. Gizzi,

- G. Grittani, S. Kar, C. H. Keitel, K. Krushelnick, S. Kuschel, S. P. D. Mangles, Z. Najmudin, N. Shukla, L. O. Silva, D. Symes, A. G. R. Thomas, M. Vargas, J. Vieira, and M. Zepf, *Nature Communications* **6**, 6747 (2015).
- [27] R. D. Edwards, M. A. Sinclair, T. J. Goldsack, K. Krushelnick, F. N. Beg, E. L. Clark, A. E. Dangor, Z. Najmudin, M. Tatarakis, B. Walton, M. Zepf, K. W. D. Ledingham, I. Spencer, P. A. Norreys, R. J. Clarke, R. Kodama, Y. Toyama, and M. Tampo, *Applied Physics Letters* **80**, 2129 (2002), <https://doi.org/10.1063/1.1464221>.
- [28] Y. Glinec, J. Faure, L. L. Dain, S. Darbon, T. Hosokai, J. J. Santos, E. Lefebvre, J. P. Rousseau, F. Burgy, B. Mercier, and V. Malka, *Phys. Rev. Lett.* **94**, 025003 (2005).
- [29] S. Steinke, J. van Tilborg, C. Benedetti, C. G. R. Geddes, C. B. Schroeder, J. Daniels, K. K. Swanson, A. J. Gonsalves, K. Nakamura, N. H. Matlis, B. H. Shaw, E. Esarey, and W. P. Leemans, *Nature* **530**, 190 (2016).
- [30] C. N. Danson, C. Haefner, J. Bromage, T. Butcher, J.-C. F. Chanteloup, E. A. Chowdhury, A. Galvanauskas, L. A. Gizzi, J. Hein, D. I. Hillier, and et al., *High Power Laser Science and Engineering* **7**, e54 (2019).
- [31] W. P. Leemans, P. Catravas, E. Esarey, C. G. Geddes, C. Toth, R. Trines, C. B. Schroeder, B. A. Shadwick, J. van Tilborg, and J. Faure, *Physical Review Letters* **89**, 1 (2002).
- [32] R. Lehe, M. Kirchen, I. A. Andriyash, B. B. Godfrey, and J.-L. Vay, *Computer Physics Communications* **203**, 66 (2016).
- [33] V. Leroux, T. Eichner, and A. R. Maier, *Opt. Express* **28**, 8257 (2020).
- [34] J. Lindström, *Linköping Studies in Health Sciences*, Ph.D. thesis, Linköping University (2011).
- [35] W. I. N. D. Huang, T. T. Allen and N. Zeng, *Journal of Global Optimization* **34** (2006), 10.1007/s10898-005-2454-3.
- [36] J. Kirschner, M. Mutny, N. Hiller, R. Ischebeck, and A. Krause, in *Proceedings of the 36th International Conference on Machine Learning*, Proceedings of Machine Learning Research, Vol. 97, edited by K. Chaudhuri and R. Salakhutdinov (PMLR, Long Beach, California, USA, 2019) pp. 3429–3438.
- [37] P. Virtanen, R. Gommers, T. E. Oliphant, M. Haberland, T. Reddy, D. Cournapeau, E. Burovski, P. Peterson, W. Weckesser, J. Bright, S. J. van der Walt, M. Brett, J. Wilson, K. Jarrod Millman, N. Mayorov, A. R. J. Nelson, E. Jones, R. Kern, E. Larson, C. Carey, Í. Polat, Y. Feng, E. W. Moore, J. VanderPlas, D. Laxalde, J. Perktold, R. Cimrman, I. Henriksen, E. A. Quintero, C. R. Harris, A. M. Archibald, A. H. Ribeiro, F. Pedregosa, P. van Mulbregt, and S. . . Contributors, *Nature Methods* **17**, 261 (2020).

VII. METHODS

A. Experimental setup

1. Plasma Source

The plasma source was a gas cell with initially 200 μm steel entrance and exit apertures. The rear aperture could translate to vary the cell length in the range of 0-10 mm. The side walls of the cell were glass slides, allowing for transverse probing of the region between the apertures. The cell was filled from below via a tube with an electronically triggered valve, which was opened for 50 ms before the laser arrival time to allow for stabilisation of the gas flow. A differential pumping system was used to remove gas after the shot in order to maintain the main vacuum chamber pressure at $\lesssim 10^{-3}$ mbar.

After the plasma source, the depleted laser was removed via a thin tape-based plasma mirror. The electrons and x-rays, generated within the plasma, passed through the thin tape to their respective diagnostics.

2. Laser

The laser was operated with a pulse energy of 245 mJ on target in a pulse duration of ~ 45 fs. The repetition rate was limited to 1 Hz to avoid the deleterious effects of heat-induced grating deformation [33]. The laser was focused at $f/18$ by a 1 m focal length off-axis parabolic mirror and was linearly polarised in the horizontal plane. The laser had a central wavelength of 803 nm and a FWHM bandwidth of 23 nm.

The on-shot temporal profile of the laser pulse was measured using a small region of the compressed pulse by spectral phase interferometry (SPIDER). The spatial phase of the laser was diagnosed with a wavefront sensor (HASO) using the small ($< 1\%$) leakage through one of the beam transport mirrors. A cross-calibrated laser profile monitor was used to measure the total laser energy of each pulse.

3. Interferometry

A ~ 1 mJ 800 nm temporally synchronised beam was used as a transverse probe of the gas cell. A 75 mm diameter 750 mm focal length collection optic was used, resulting in a minimum resolution of 9.7 μm . A folded wavefront Michelson interferometer was used to provide on-shot measurements of the plasma density when the gas cell length was > 1.7 mm.

4. Electron Spectrometer

The spectrum of the generated electron beams was measured using a magnetic spectrometer consisting of a permanent dipole magnet with a peak magnetic field of 558 mT, a scintillating Lanex screen ($\text{Gd}_2\text{O}_2\text{S:Tb}$, [34]) and an Allied Vision Manta G-235B camera, all sealed in a light-tight lead box. The charge calibration was performed using Fuji BAS-MS2325 image plate. The magnet entrance was 574 mm from the electron source and the total length of the spectrometer was 410 mm. The energy range of the spectrometer, for electrons propagating along the axis was 26 MeV - 218 MeV.

5. X-ray Diagnostic

X-rays were diagnosed with a direct detection x-ray CCD (Andor iKon-M 934) attached to an on-axis vacuum flange placed 1.23 m from the x-ray source. To prevent laser light from reaching the CCD, two sheets of 12.8 μm thick Mylar foil, coated with 400 nm Al on the front surface and 200 nm Al on the back surface, was used to cover the entrance aperture. This had the additional effect of blocking out 99.6% of x-rays below 1.6 keV (K-edge of Al). The x-ray spectrum was retrieved by comparing the transmission through different materials according to [4]. The materials chosen were $(33.5 \pm 1.1) \mu\text{m}$ Al(98%)/Mg(1%)/Si(1%), $(29.5 \pm 0.3) \mu\text{m}$ Al(95%)/Mg(5%), $(20.15 \pm 0.45) \mu\text{m}$ Mg, $(21.85 \pm 0.25) \mu\text{m}$ Mylar and $(12.9 \pm 0.1) \mu\text{m}$ Kapton, which were mounted on $(12.85 \pm 0.25) \mu\text{m}$ Mylar, and all coated with 200 nm Al to prevent oxidation. Additionally, a 50 μm tungsten filter provided the on-shot background signal.

For the optimal burst of the optimisation in fig. 3, the x-ray spectrum was fitted with a synchrotron spectrum with a critical energy of $E_c = 2.7 \pm 0.9$ keV and contained $(1.3 \pm 0.7) \times 10^3$ photons mrad^{-2} above 1.6 keV.

B. Bayesian Optimisation Algorithm

The fitting algorithm comprised of two independent Gaussian process models. The first took the position X_m , mean value \bar{Y}_m and variance ϵ_m^2 of each measurement and created a model capable of predicting the mean $\bar{Y}(X)$ of the objective function with standard deviation $\sigma(X)$. As the measured values of ϵ_m are a noisy estimation of the true variance $\epsilon(X)^2$, a second Gaussian process model took the values of X_m and ϵ_m in order to predict the true standard deviation of the objective function $\epsilon(X)$.

The covariance kernel for both GPR models was expressed as a radial basis function added to a white-noise-function. The physical measurement positions were each individually scaled to values that varied by similar amounts, so that the kernels would be approximately

isotropic. The hyperparameters of the kernel were optimised during the fitting process by maximising the marginal likelihood of each.

The two models were combined in order to provide an estimation of the sampling efficiency at any given position. Per [35], this can be represented by a term:

$$\eta = 1 - \frac{\epsilon}{\sqrt{\sigma^2 + \epsilon^2}} \quad (1)$$

where ϵ is the uncertainty of each measurement, while σ is the standard deviation of the Gaussian process model. This was multiplied by the standard expected improvement acquisition function to produce an *augmented* acquisition function. In extensively-sampled regions, as σ approaches 0 so does η . On the other hand, where experimental errors are dominated by the model uncertainty, η is close to 1.

In addition, the white-noise kernel adds to the model standard deviation σ when it should be counted as part of the experimental error ϵ . This affects the behaviour of the acquisition function, and crucially of the term η . So when calculating the augmented acquisition function the variance of the white-noise term was subtracted from the model variance and added to the experimental variance.

Finding the maximum of the acquisition function is a further optimisation problem, but of a function which has many local optima. Evaluation positions for the acquisition function were selected by a series of line segments generated in random directions through existing samples. Each line segment is uniformly sampled, and the maximum of the acquisition function over all points from all lines was used for the next measurement. This approach was inspired by, but is substantially different from, a published solution to the same problem [36], in which a multi-dimensional optimisation problem was reduced to a sequence of 1D optimisations in random directions.

1. Computation time for Bayesian optimisation algorithm

Each iteration of the Bayesian optimisation algorithm required two computationally expensive steps.

1. Fitting of the Gaussian process models to the measurements
2. Finding the maximum of the acquisition function

The execution time of both steps increases approximately linearly with the number of measurements. On a PC with a Intel Xeon Processor E5-1620 v3 3.5 GHz CPU and 64 GB of 2.1 GHz RAM, step 1 took 260 ms and step 2 took 290 ms after 50 measurements. Note that maximising the acquisition function is another optimisation problem which involves multiple evaluations of the acquisition function. For the results of this paper, including the execution time given above, 20,000 function evaluations were used to maximise the acquisition function.

C. Comparison of optimisation algorithms

Alternative optimisation algorithms can be tested using the same surrogate model shown in fig. 5a, by sampling from the final distribution. These synthetic measurements were then used as the objective function for the alternative optimisation algorithm. Each algorithm (except grid search) was performed > 100 times and was initialised from a randomised starting point in parameter space. The convergence was calculated by taking the average of the model prediction at each optimal point found by the optimisations as a fraction of the global optimum. The Bayesian optimisation model used in the experiment reached an average of 94% of the model optimum with 60 measurements. By comparison, $4\times$ sequential 1D scans achieved 80% convergence using the same number of measurements (15 measurements per axis). A genetic algorithm (SciPy differential evolution [37]) achieved 69% convergence in 60 measurements. A Nelder-Mead algorithm (also from the SciPy library) achieved 34% convergence using 60 measurements. A 4D grid search obtained 95% convergence using 14641 measurements (11 measurements per dimension). It should be acknowledged that the convergence of any of these algorithms could be improved through tuning of the algorithms and their hyperparameters.

D. Particle-in-cell simulations

Simulations were performed using the particle-in-cell code FBPIC. FBPIC uses cylindrical symmetry with azimuthal mode decomposition which is well suited to situations close to cylindrical symmetry. For the simulations in this paper, two azimuthal modes were used, over a simulation window of $80 \times 80 \mu\text{m}$ in 1600×100 cells in the z and r directions respectively. The electron density profile used was based on fluid modelling of the gas density profile using the code OpenFOAM. This gave entrance and exit density ramps that fell to half of the maximum density over a distance of $700 \mu\text{m}$ and $850 \mu\text{m}$ respectively and a plateau of uniform density of length 1 mm starting at $z = 2 \text{ mm}$. The plasma was initialised with He^{1+} and N^{5+} ions with a free electron species neutralising the overall charge density. The initial electron density in the plateau was $1.26 \times 10^{19} \text{ cm}^{-3}$. Each species used $2 \times 2 \times 8$ macro-particles in the $z \times r \times \theta$ directions. Ionisation is handled in FBPIC by an algorithm based on ADK ionisation rates. The laser pulse was initialised to match the experimental measurements of laser energy, spectral intensity and phase and intensity distribution at the focal plane. The laser pulse spatial phase and intensity distribution were then modified to ensure focusing in vacuum would occur at the start of the density plateau.

VIII. DATA AVAILABILITY

The data presented in this paper and other findings of this study are available from the corresponding authors upon reasonable request.

IX. ACKNOWLEDGEMENTS

The authors gratefully acknowledge the hard work of the staff at the Central Laser Facility in the planning and execution of the experiment. R.J.S., J-N.G., M.B., S.P.D.M., Z.N. and M.J.V.S. acknowledge funding from Science and Technology Facilities Council Grant No. ST/P002021/1 and the EU Horizon 2020 research and innovation programme grant No. 653782. A.G.R.T acknowledges funding from US NSF grant numbers 1804463 and DE-SC0020237. A.G.R.T and K.K. acknowledge funding from US DOE/High Energy Physics grant number DE-SC0016804. C.T. acknowledges funding from the Engineering and Physical Sciences Research Council grant number EP/S001379/1.

X. AUTHOR CONTRIBUTIONS

All authors contributed to the planning and execution of the experiment. R.J.S., J-N.G., C.I.D.U. and M.J.V.S. performed analysis. S.J.D.D. developed the software framework for experimental automation. S.J.D.D., R.J.S. and M.J.V.S. wrote the experimental control and analysis algorithms. S.J.D.D. and M.J.V.S. wrote the Gaussian process regression interface using the Scikit-learn interface. C.A. and M.J.V.S. performed PIC simulations. R.J.S., J-N.G., S.J.D.D. and M.J.V.S. wrote the paper with contributions from all authors.